Adaptive Constraints Model Active Mismatch Predictive Control for Power Converters of Energy Storage System

Xibeng Zhang, *Member, IEEE*, Shun Zhou, Benfei Wang, *Senior Member, IEEE*, Yang Lu, Yanyu Zhang, Feng Huo, Darong Huang, *Member, IEEE*, and Abhisek Ukil, *Senior Member, IEEE*

***Abstract*—Model predictive control (MPC) is widely employed for power converters in energy storage systems. However, the limited sampling frequency of microcontrollers and model mismatches can cause trajectory tracking errors in both dynamic and steady states, potentially damaging electrical equipment and reducing the lifespan of electrical devices. To address these issues, this article proposes an adaptive constraints model active mismatch predictive control (AC-MAMPC) method for power converters. The inductance and capacitance values of the system model can be actively adjusted in the state-space model to eliminate current ripple caused by control delays. For model mismatches resulting from the proposed active model mismatch mechanism and perturbations, an adaptive constraints method for online optimization of MPC is introduced to handle plant model mismatches without updating model parameters. The performance of the proposed method is validated through simulation and hardware experiments.**

***Index Terms*—Active mismatch, adaptive constraints, current ripple, model mismatch, model predictive control (MPC).**

I. Introduction

THE future power system will integrate more distributed microgrids, consisting of renewable energy sources and various types of energy storage systems (ESS) [1]. To balance power between generation and load, power electronic devices are employed to achieve the charging and discharging of ESS. Therefore, developing efficient control strategies for ESS power converters is crucial to maintaining the stable operation of microgrids.

Received 12 December 2024; revised 4 April 2025; accepted 14 May 2025. Date of publication 19 May 2025; date of current version 30 June 2025. This work was supported in part by the Special Project of the National Natural Science Foundation under Grant 42341204, in part by the Henan Science and Technology Research Project of China under Grant 232102241021, in part by the ChunHui Project under Grant 202200811, and in part by the Guangdong Basic and Applied Basic Research Foundation under Grant 2024A1515011059. Recommended for publication by Associate Editor F. D. Freijedo. *(Corresponding author: Benfei Wang.)*

Xibeng Zhang is with Henan University, Kaifeng 475001, China, and also with Longzihu New Energy Laboratory, Zhengzhou 450000, China (e-mail: xbzhang@henu.edu.cn).

Shun Zhou, Yang Lu, and Yanyu Zhang are with Henan University, Kaifeng 475001, China (e-mail: zhoushun@henu.edu.cn; lykyc@henu.edu.cn; zyy@henu.edu.cn).

Benfei Wang is with Sun Yat-Sen University, Guangzhou 510275, China (e-mail: wangbf8@mail.sysu.edu.cn).

Feng Huo is with the Beijing Key Laboratory of Ionic Liquids Clean Process, Institute of Process Engineering, Chinese Academy of Sciences, Beijing 100190, China, and also with Longzihu New Energy Laboratory, Zhengzhou 450000, China (e-mail: huofeng@ipe.ac.cn).

Darong Huang is with Anhui University, Hefei 230601, China (e-mail: drhuangjs@ahu.edu.cn).

Abhisek Ukil is with University of Auckland, Auckland 1142, New Zealand (e-mail: a.ukil@auckland.ac.nz).

Color versions of one or more figures in this article are available at https://doi.org/10.1109/TPEL.2025.3571252.

Digital Object Identifier 10.1109/TPEL.2025.3571252

A. Literature Review

Model predictive control (MPC) is well-suited for multiple-input multiple-output nonlinear plants with complex dynamics [2], making it widely used for controlling power converters over the past decade. The cost function in MPC is formulated by comparing the target value with predicted system states, allowing the future behavior of the power converter to be predicted based on mathematical models [3]. Therefore, an accurate model of the power converter is essential for predicting its system states. Shan et al. [4] model the dc–dc converter for both switch-ON and switch-OFF modes under ideal conditions, with switch actions (OFF or ON) obtained directly by solving the cost function. In [5], the state-space averaging method is used to model converters, considering uncertain modeling errors as system states in the modeling process. The system model proposed in [6] includes different modes of switch operations, accounting for the nonlinear behavior of dc–dc converters, with disturbances regarded as additive white Gaussian noise. For ESS modeling, Song et al. [7] actively injected signals into the model battery to improve the estimation accuracy of battery states.

In addition, various research works aim to improve the control performance of MPC by enhancing the control mechanism. The paper presented in [8] introduces a two-stage MPC method for flying capacitor converters to reduce dynamic error by considering current tracking error and the balance of floating capacitors. Liu et al. [9] proposed a hybrid MPC and PI controller for hybrid energy storage system (HESS), where MPC generates the current reference for the battery and supercapacitor (SC), and PI controllers track these references. Zhou and Preindl [10] presented a variable switching frequency MPC with constant sampling time, where the carrier wave frequency is obtained by a frequency controller to ensure critical soft switching operation, and the duty ratio of the converter is generated by the MPC controller. In [11], the tracking error in each control interval is used to update the tracking reference to eliminate dynamic error.

The work in [12] employs nonlinear inductors in dc–dc converters to achieve faster power transfer, with Luenberger observers estimating the parameters of nonlinear inductors for modeling the predictive mode. The research work in [13] constructs a virtual capacitance in the system model to make the predicted value of MPC tolerate the effect of noise. However, there are still challenges in applying MPC methods to power converters of ESS.

1) *Model mismatch problem*: DC–DC converters exhibit unmodeled dynamics, which can lead to a mismatch between the mathematical model and the physical plant.
2) *Control delay problem*: MPC method has a one-step control delay, especially when the sampling frequency of the microcontroller is limited, can affect control performance.

For model mismatch problems, disturbance observer-based methods and model-free MPC strategies are two common approaches to mitigate the influence of physical parameters. Disturbance observer-based methods address parameter variations by observing and compensating for disturbances caused by model mismatch. In [14], the system matrix is identified using the recursive least squares method. To enhance robustness against machine parameter mismatch, Niu et al. [15] used sliding mode to estimate inductance and flux mismatch. Tao et al. [16] proposed an active disturbance rejection control scheme to address unknown dynamics and external disturbances. These uncertainties are compensated for in the control law to enhance dynamic performance. Panda and Subudhi [17] introduced a robust distributed secondary control strategy for voltage and frequency regulation in islanded microgrids via voltage source inverters. This approach employs an extended state observer (ESO) to estimate disturbances and guarantee system stability. Model-free MPC [18], [19], [20], on the other hand, uses only the input/output data of the controlled plant instead of a dynamic model structure to determine control signals. The research proposed in [18] utilizes an event-triggered mechanism to reduce switching losses, and a fuzzy logic system is used to approximate the ultralocal mathematical model of converters to address uncertainties and tracking errors. In [19], an ultralocal model for power converters is deduced, where parameter mismatches are considered as lumped disturbances, which can be estimated using current and voltage data from the last control period. The ESO framework can also be extended to model-free MPC, in [20], the linear ESO takes the unknown parts as state variables, and the predicted value of the system state can be estimated by ESO. Similarly, Babayomi et al. [21] introduced a parallel-cascade ESO combined with model-free MPC to control dc–dc boost converters, improving measurement noise suppression. While disturbance observer-based methods and model-free MPC demonstrate strong robustness against disturbances, they still face challenges such as parameter tuning during implementation and persistent one-step control delays.

For the one-step control delay problem, Zhang et al. [11] calculated the voltage vector reference at the kth moment based on the assumption that the system state can track the reference voltage vector at $(k+2)$th moment instead of $(k+1)$th moment. In [22], the error between the actual output voltage and the estimated voltage value caused by control delay is considered in the cost function of MPC. In [23], the predicted variables are obtained using a data-driven model, and an ESO is adopted to obtain more accurate stator currents considering delays. In the work proposed in [24], the time delay is calculated based on the sampling currents, and the current variation caused by the control delay is predicted and used to compensate the control actions. However, these delay compensation methods require a precise mathematical model of the converters.

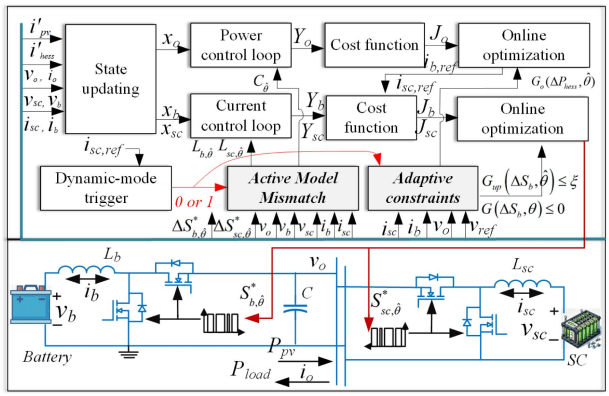

Fig. 1. Control strategy of AC-MAMPC.

B. Main Contributions of This Article

Motivated by the aforementioned discussions, the research gap can be summarized that the existing control methods in dc–dc converters encounter issues including high control system complexity, the necessity for precise mathematical models, and difficulties in parameter tuning when addressing control delay and model mismatch problems. For these issues, this article presents an adaptive constraints model active mismatch predictive control (AC-MAMPC) method for power converters of ESS to compensate for tracking errors caused by one-step control delay and model mismatch. As the most commonly used structure of HESS, battery-SC and basic bidirectional dc–dc converters are used as the controlled system in this article. The main contributions of this article can be summarized as follows.

1) An active model mismatch mechanism that operates with linear ideal models is presented to mitigating the impact of control delay and disturbances on performance.
2) To deal with plant-model mismatch problem, the constraints of optimization can adaptive variation instead of updating the system parameters and it only requires the feedback information.

II. System Description and Conventional MPC (C-MPC) Method

The structure of an islanding microgrid with an HESS is shown in Fig. 1. HESS, photovoltaic (PV) panel, and dc load are connected with dc bus through dc–dc converters. Here, $i_{\rm sc}$, i_b, $i_{\rm pv}$, and i_o are the current of SC, battery, PV panel, and load, respectively. v_b and $v_{\rm sc}$ are the voltage of battery and SC. L_b, S_b, $L_{\rm sc}$, $S_{\rm sc}$ are the inductance and duty ratio of power converters. C

is the equivalent capacitance on dc bus. v_o is the output voltage of dc bus.

To keep the power balance of microgrid, the control strategy of HESS should take over the charging and discharging behaviors of HESS to provide or absorb the power. In C-MPC method [25], [26], the power control loop (or voltage control loop) is formulated according to power balance equations, and the discrete difference equations share shown that

$$\begin{cases} v_o(k+1) = v_o(k) + \frac{t_s}{C}\left(i'_{\text{hess}}(k) + i'_{\text{pv}} - i_o(k)\right) \\ P_{\text{loss}}(k+1) = P_{\text{loss}}(k) \end{cases} \tag{1}$$

where t_s is the sampling time. $i'_{\text{hess}}(t)$, $i'_{\text{pv}}(t)$ are the dc–dc output current of HESS and PV, and $i'_{\text{hess}} + i'_{\text{pv}} = (P_{\text{pv}} + P_{\text{hess}} - P_{\text{loss}})v_o{}^{-1}$. P_{hess}, P_{pv} are the power of HESS and PV. P_{loss} is the power losses of energy conversion. Setting P_{hess} and v_o as the control variable and output variables, and the system state is $x_o = [\Delta v_o \quad \Delta P_{\text{loss}} \quad v_o]^T$. The N_p-dimensional matrix Y_o represents the predicted value of v_o: $Y_o = [v_o(k+1) \quad v_o(k+2) \quad \cdots \quad v_o(k+N_p)]^T$, and N_p is the predictive horizon. Y_o is obtained by (1), it can be expressed as

$$Y_o = Q_o x_o(k) + \phi_o \Delta P_{\text{hess}} \tag{2}$$

where Q_o and ϕ_o are the predictive matrix acquired by augmented state-space model. In the power control loop, voltage regulation is achieved by controlling Y_o to track the reference output voltage V_{ref} while minimizing variations in the control action ΔP_{hess}. Accordingly, the cost function can be formulated as

$$J_{o,\theta} = (V_{\text{ref}} - Y_o)^T (V_{\text{ref}} - Y_o) + \Delta P_{\text{hess}} \bar{R}_1 \Delta P_{\text{hess}}^T \tag{3}$$

where θ represents the nominal values of system parameters. $\bar{R}_1$ is the optimization coefficient. The current references of battery and SC, denoted as $i_{b,\text{ref}}$ and $i_{\text{sc,ref}}$, are derived from optimal power reference of HESS $P^*_{\text{hess},\theta}$, which is obtained by minimizing (3)

$$i_{b,\text{ref}} = \frac{f_{\text{lpf}}\left(P^*_{\text{hess},\theta}\right)}{v_b}, i_{\text{sc,ref}} = \frac{P^*_{\text{hess},\theta} - f_{\text{lpf}}\left(P^*_{\text{hess},\theta}\right)}{v_{\text{sc}}} \tag{4}$$

where $f_{\text{lpf}}(\bullet)$ is the one-order low-pass filter. SC is employed to handle high-frequency power fluctuations due to its high power density, enabling rapid charge/discharge cycles for dynamic power compensation.

In the current control loop, the system models are

$$\begin{cases} i_b(k+1) = i_b(k) + \frac{t_s}{L_b}\left(v_b(k) - (1 - S_b(k))v_o(k)\right) \\ v_b(k+1) = v_b(k) \end{cases} \tag{5}$$

where S_b are the duty ratio of power converters connected with battery, and the system state is $x_b = [\ \Delta i_b \quad \Delta v_b \quad i_b\ ]^T$. Similarly, the cost function of battery current control loop is

$$\begin{aligned} J_{b,\theta} &= (i_{b,\text{ref}} - Y_b)^T (i_{b,\text{ref}} - Y_b) + \Delta S_b \bar{R}_2 \Delta S_b^T \\ &= \frac{1}{2}\Delta S_b^T E_b \Delta S_b + \Delta S_b F_b \\ &\begin{cases} E_b = 2\left(\phi_b{}^T \phi_b + \bar{R}_2\right) \\ F_b = 2\phi_b{}^T \left[i_{b,\text{ref}} - Q_b x_b(k)\right] \end{cases} \end{aligned} \tag{6}$$

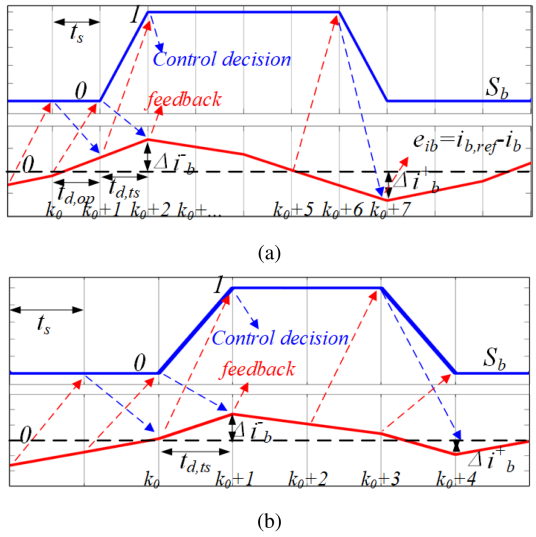

Fig. 2. (a) Current ripple caused by control delay in steady state. (b) Current ripple caused by control delay in steady state under the active model mismatch.

where Y_b is the predicted values of i_b, ϕ_b is the parameter matrix obtained by substituting into and simplifying (5), and $\bar{R}_2$ is the weight of the cost function. For the constraint of the optimization problem, the duty ratio should be less than 1: $0 \le S_b \le 1$. Also, i_b and state of charge (SOC) of battery should be maintained within the safe range. The duty ratio of power converters S_b can be obtained by minimizing (6).

In the SC current control loop, the system model can be shown as

$$\begin{cases} i_{\text{sc}}(k+1) = i_{\text{sc}}(k) + \frac{t_s}{L_{\text{sc}}}\left(v_{\text{sc}}(k) - (1 - S_{\text{sc}}(k))v_o(k)\right) \\ v_{\text{sc}}(k+1) = v_{\text{sc}}(k) + \frac{t_s}{C_{\text{sc}}}\left(i_{\text{sc}}(k)\right) \end{cases} \tag{7}$$

where S_{sc} are the duty ratio of power converters connected with SC, and the system state is $x_{\text{sc}} = [\Delta i_{\text{sc}} \quad \Delta v_{\text{sc}} \quad i_{\text{sc}}]^T$. The cost function of SC current control loop $j_{\text{sc},\theta}$ are designed as same as that of battery current loop.

III. Active Model Mismatch Mechanism

A. Analysis of Control Delay and Model Mismatch Problem

C-MPC method introduced in Section II is able to maintain the output voltage as V_{ref}, however, the control delay would increase current ripple and voltage fluctuation, and model mismatch problem would also affect control performance.

The control delay time t_d is consist of sampling time delay t_{d,t_s} and optimization delay $t_{d,\text{op}}$

$$t_d = t_{d,t_s} + t_{d,\text{op}}. \tag{8}$$

Fig. 2(a) shows the processing about how the control delay lead to current ripple, where optimization delay $t_{d,\text{op}}$ is caused by the online optimization of MPC. To analyze the optimization delay formation, consider the case where all MPC constraints (except the duty ratio range) remain inactive. Under this condition, the system output depends solely on the duty ratio. At k_0,

i_b is close to $i_{b,\text{ref}}$, the following relationship holds:

$$|e_{ib}(k_0)| < \left|\Delta i^-_{b,t_s}\right| \tag{9}$$

where $|\Delta i^-_{b,t_s}|$ is the maximum current falling within single sampling period t_s, when the duty ratio is maintained at 1

$$\left|\Delta i^-_{b,t_s}\right| = \frac{t_s}{L_b}\left(v_o(k_0) - v_b(k_0)\right). \tag{10}$$

At k_0+1, since the tracking error is less than maximum current variation, the constraint about duty ratio is an inactive constraint, and the optimization problem of (6) becomes an unconstrained problem, hence the optimal control actions can be obtained by minimizing $J_{b,\theta}$

$$\frac{dJ_{b,\theta}}{dS^*_b} = 0, \Delta S^*_{b,\theta} = -E_b^{-1}F_b. \tag{11}$$

Due to $i_b(k_0)$ is close to $i_{b,\text{ref}}$, it has: $i_{b,\text{ref}} - Q_b x_b(k_0) \approx 0$. According to (6), F_b and the global optimal solution calculated at k_0 can be calculated

$$\begin{aligned} &F_b|_{k=k_0} = 0 \\ &\Delta S^*_{b,\theta}(k_0+1) = 0. \end{aligned} \tag{12}$$

At k_0+1, the unchanged control action at k_0 results in a one-step delay in responding to the tracking error, which is shown in (13), where ω_i is the random disturbance in current control loop. This one-step delay is referred to as the optimization delay $t_{d,\text{op}}$ in this article

$$e_{ib}(k_0+1) = \frac{t_s}{L_b}\left(v_o - v_b + \omega_i\right) - |e_{ib}(k_0)|. \tag{13}$$

So, the magnitude of $|\Delta i^-_{b,t_s}|$ and $|\Delta i^+_{b,t_s}|$ dictates the current ripple induced by optimization delay.

Sampling time delay t_{d,t_s} caused by the one-step unsynchronization between control action and system state. The control action decided at k_0+n based on the feedback information at k_0+n-1, and it works at k_0+n+1, which would cause the current ripple. Neglecting the inductor current waveform caused by switching actions, the current ripple caused by control delay problem can be calculated that

$$\begin{aligned} \Delta i_{b,\theta} &= \left|\Delta i^-_b\right| + \left|\Delta i^+_b\right| \\ &= 2\frac{t_s}{L_b}\left(v_o + \omega_i\right) - |e_{ib}(k_0)| - |e_{ib}(k_0+5)|. \end{aligned} \tag{14}$$

The current ripple $\Delta i_{b,\theta}$ induces additional voltage fluctuation of magnitude $\frac{t_s}{C}\Delta i_{b,\theta}$.

Furthermore, model mismatch degrades control performance. As shown in (10), the falling of inductance in system model, $L_{b,\hat\theta} = L_b - \Delta L_b$, would increase both the maximum current deviations ($|\Delta i^-_{b,t_s}|$ and $|\Delta i^+_{b,t_s}|$), consequently, and the current ripple would be increasing comparing with (14)

$$\Delta i_{b,\hat\theta} = \Delta i_{b,\theta} + \frac{\Delta L_b}{L_b - \Delta L_b}\left(v_o - v_b\right). \tag{15}$$

In contrary, as shown in Fig. 2(b), increasing the inductance in the system model reduces the current ripple caused by optimization delay. This occurs because higher inductance makes the MPC more sensitive to small tracking errors, leaving only the sampling delay-induced current ripple. However, v_o at the instant when the control system initiates current decay will be larger than when it initiates current rise, according to (10), it has

$$\left|\Delta i^-_{b,t_s}\right|\left(1 - S_{b,\hat\theta}\right) > \left|\Delta i^+_{b,t_s}\right| S_{b,\hat\theta}. \tag{16}$$

Hence, comparing with the current reference $i_{b,\text{ref}}$, the maximum current falling ripple $|\Delta i^-_b|$ is larger than the maximum current rising ripple $|\Delta i^+_b|$, introducing steady-state tracking error.

Analogously, in the power control loop, reduced capacitance amplifies voltage fluctuations while increased capacitance lead to voltage steady-state error.

B. Updated Algorithm of Inductance Active Model Mismatch

According to the analysis in Section III-A, the sampling time delay and optimization delay would cause additional current ripple. To compensate the control delay, this article introduces disturbances to the inductance of dc–dc converters

$$\begin{aligned} &L_{b,\hat\theta} = L_{b,\theta} + \hat\theta_1 \\ &L_{\text{sc},\hat\theta} = L_{\text{sc},\theta} + \hat\theta_2 \\ &\hat\theta_1, \hat\theta_2 > 0. \end{aligned} \tag{17}$$

The generation process of current ripple under active model mismatch mechanism is shown in Fig. 2(b). To eliminated the optimization delay, the inequality constraints of the optimization problem should be active when i_b is close to $i_{b,\text{ref}}$, so the magnitude of $\Delta i^-_{b,t_s}|_{s_b=0}$ and $\Delta i^+_{b,t_s}|_{s_b=1}$ should be reduced by adjusting the system model. The current ripple with the active inductance disturbance can be written as

$$\begin{aligned} \Delta i_{b,\hat\theta} &= \frac{t_s}{L_{b,\hat\theta}}\left(v_o + \omega_i\right) - |e_{ib}(k_0)| - |e_{ib}(k_0+3)| \\ \Delta i_{b,\hat\theta} &< \Delta i_{b,\theta}. \end{aligned} \tag{18}$$

So the current ripple can be reduced. Similarly, the active model mismatch on L_{sc} can eliminate the current ripple of SC current. According to the switching characteristics of power converter, in continuous current mode, the maximal current change in steady state can be written as

$$\Delta i_{b,\max} = \frac{t_s}{L_{b,\theta}}\left(1 - D_b\right) D_b v_o \tag{19}$$

where D_b is the duty ratio of the power converter at static operation points. Hence, the disturbances on inductance should follow

$$\frac{t_s}{L_{b,\theta}\frac{L_{b,\hat\theta}}{L_{b,\theta}}}\left|\left(v_b(k) - \left(1 - S_b(k)\right)v_o(k)\right)\right| \geq \Delta i_{b,\max} \tag{20}$$

Substituting (19) to (20), the active disturbances on inductance should be

$$\frac{L_{b,\hat\theta}}{L_{b,\theta}} \leq \frac{\left(1 - D_b\right) D_b v_o(k)}{\left|\left(v_b(k) - \left(1 - S_b(k)\right)v_o(k)\right)\right|}. \tag{21}$$

To reach the minimal current ripple, $\hat{\theta}_1$ should be selected as the maximum within the range shown in (21). However, the active disturbances on inductance would cause the tracking error in current control loop, especially if the current level of HESS is low, the tracking error in current control loop would lead to larger steady-state error on dc bus voltage, which would bring more challenge for model mismatch compensation. So the current adaptive factor $\alpha e^{-i_b(k)}$ is introduced to address this problem, and α is a constant and $\alpha \in (0, 0.5)$, the selection of α is based on the voltage conversion rate of power converter. Hence, the updated algorithm of inductance active model mismatch is

$$\hat{\theta}_1 = L_{b,\theta}\left(\frac{(1-D_b)\,D_b v_o(k)}{\left|(v_b(k)-(1-S_b(k))\,v_o(k)\right|} - \alpha e^{-i_b(k)} - 1\right). \tag{22}$$

Also, $L_{\mathrm{sc},\hat{\theta}}$ and $\hat{\theta}_2$ can be obtained by the same way. The cost functions in current control loop under the active model mismatch is shown

$$\begin{aligned} J_{b,\hat{\theta}} &= \frac{1}{2}\Delta S_b^T E_{b,\hat{\theta}} \Delta S_b + \Delta S_b F_{b,\hat{\theta}} \\ J_{\mathrm{sc},\hat{\theta}} &= \frac{1}{2}\Delta S_{\mathrm{sc}}^T E_{\mathrm{sc},\hat{\theta}} \Delta S_{\mathrm{sc}} + \Delta S_{\mathrm{sc}} F_{\mathrm{sc},\hat{\theta}}. \end{aligned} \tag{23}$$

IV. Proposed AC-MAMPC

A. Analysis of Model Mismatch Problem in Current Control Loop

Model mismatch can reduce the tracking accuracy of MPC control, and the active model mismatch mechanism introduced in last section would bring additional mismatch problems. To address this issue, an adaptive constraints method is proposed in this section.

The optimization problem for the system model with normal value can be expressed as

$$\begin{aligned} \arg\min \quad & J_{b,\theta} = \frac{1}{2}\Delta S_b^T E_b \Delta S_b + \Delta S_b F_b \\ \text{s.t} \quad & G\left(\Delta S_b, \theta\right) \le 0. \end{aligned} \tag{24}$$

Assuming the optimal problem (24) satisfy the KKT conditions, and it has unique Lagrange multipliers and optimal solution $\Gamma_\theta = [\lambda_\theta^* \quad \Delta S_{b,\theta}^*]^T$.

According to the basic sensitivity theorem proposed in [27], there existing unique $\Gamma_{\hat{\theta}} = [\lambda_{\hat{\theta}}^* \quad \Delta S_{b,\hat{\theta}}^*]^T$ for the optimization problem with disturbance $\hat{\theta} = \theta + \Delta\hat{\theta}$

$$\begin{aligned} &\arg\min J_{b,\hat{\theta}} = \frac{1}{2}\Delta S_b^T E_{b,\hat{\theta}} \Delta S_b + \Delta S_b F_{b,\hat{\theta}} \\ &\text{s.t}\, G\left(\Delta S_b, \theta\right) \le 0 \\ &G\left(\Delta S_b, \hat{\theta}\right) = M\Delta S_b - \eta \end{aligned} \tag{25}$$

where $M\Delta S_b \le \eta$ is the matrix of constraints. According to dual feasibility conditions, it has

$$f_1 : \nabla J_{b,\hat{\theta}} + \sum_{j \in G_{\mathrm{act}}} \lambda_{\hat{\theta},j}^* \nabla G_j\left(\Delta S_{b,\hat{\theta}}^*, \hat{\theta}\right) = 0 \tag{26}$$

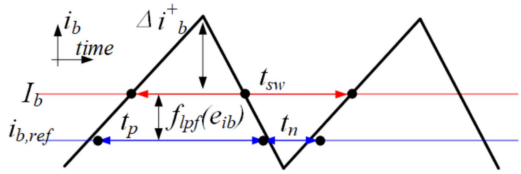

Fig. 3. Steady-state error caused by model mismatch.

where G_{act} is the set of active constraints. Hence, the changing of $\Gamma_{\hat{\theta}}$ with the variation of model mismatch $\Delta\hat{\theta}$ can be expressed as

$$\Delta\hat{\theta} \cdot \frac{\partial f_1}{\partial \hat{\theta}} = -\left[\frac{\partial f_1}{\partial \lambda_{\hat{\theta}}^*}\Delta\lambda_{\hat{\theta}}^* + \frac{\partial f_1}{\partial \Delta S_{b,\hat{\theta}}^*}\Delta\left(\Delta S_{b,\hat{\theta}}^*\right)\right]. \tag{27}$$

Hence, to compensate the model mismatch $\Delta\hat{\theta}$, $\Gamma_{\hat{\theta}}$ should change following (27).

B. Updated Algorithm of Adaptive Constraints

The active model mismatch mechanism presented in Section III contributes to the model mismatch $\Delta\hat{\theta}$. In addition, system nonlinearities, dynamic power losses, component parameter variations, and random disturbances also contribute to $\Delta\hat{\theta}$. Consequently, it is challenging to determine $\Gamma_{\hat{\theta}}$ directly based on (27). While, the Lagrange multipliers and optimal solution can be calculated based on the set of active constraints G_j

$$\begin{aligned} \lambda_{\hat{\theta},j}^* &= -\left(M_j E_{b,\hat{\theta}}^{-1} M_j^T\right)^{-1}\left(\eta_j + M_j E_{b,\hat{\theta}}^{-1} F_{b,\hat{\theta}}\right) \\ \Delta S_{b,\hat{\theta}}^* &= -E_{b,\hat{\theta}}^{-1}\left(F_{b,\hat{\theta}} + M_j^T \lambda_{\hat{\theta},j}^*\right) \\ & j \in G_{\mathrm{act}}. \end{aligned} \tag{28}$$

Hence, $\Gamma_{\hat{\theta}}$ can be acquired by adjusting the active constraints to compensate the model mismatch.

Since constraints about current limitation and SOC are inactive constraints in most cases under the steady state, the set of active constraints depend on constraints about duty ratio. The adaptive duty ratio constraint is designed as

$$G_{\mathrm{up}}\left(\Delta S_b, \hat{\theta}\right) \le -\xi \tag{29}$$

where G_{up} is the upper limit for duty ratio, ξ is the adaptive factor. The updated law of adaptive factor is shown as

$$\xi(k) = \xi\left(k-1\right) + B \cdot \mathrm{sign}\left[\frac{f_{\mathrm{lpf}}\left(e_{ib}(k)\right)}{e_{ib}(k)}\right] \tag{30}$$

where B is the updated parameter. Fig. 3 shows the negative steady-state error caused by model-mismatch, t_{sw} is the switching period.

Theorem 1: If the optimal problem with normal value has unique optimal solution $\Delta S_{b,\theta}^*$, there is existing B that making the constraint convergence at the active constraint G_j for $\Delta S_{b,\hat{\theta}}^*$ when $\xi(k) = \lim_{k\to+\infty}\xi(k)$.

Proof: According to (30), during the single switching period when $f_{\mathrm{lpf}}(e_{ib})$ is negative, the changing of adaptive factor

is

$$\Delta\xi = B \cdot \underbrace{\frac{\frac{t_{sw}}{\Delta i_b^+}\left|f_{lpf}\left(e_{ib}\right)\right| + t_{sw}}{2}}_{t_p} - B \cdot \underbrace{\left(t_{sw} - t_p\right)}_{t_n}. \tag{31}$$

Since $t_p > t_n$ when the steady-state error is negative, and ξ keeps increasing, so the duty ratio at steady-state become $D \to D(1-\xi)$, according to small signal model of dc–dc converter

$$L\frac{d\hat{i}}{dt} = \hat{v}_b + \left(1 - D\left(1-\xi\right)\right)\hat{v}_o - V_o\hat{d}. \tag{32}$$

The average battery current I_b will decrease with the increasing of ξ, and t_p would decrease based on (31).

To maintain the constraint convergence at active constraints, when $f_{lpf}(e_{ib})$ is negative, t_p should be always greater than or equal to t_n. Since

$$t_p\left(k+1\right) = \frac{t_{sw}\left(\left|f_{lpf}\left(e_{ib}(k)\right)\right| - \Delta I_b\left(k+1\right) + \Delta i_b^+\right)}{2\Delta i_b^+}$$

$$t_{sw} = t_p + t_n. \tag{33}$$

To keep $t_p \geq t_n$, the inequality (34) should be satisfied

$$\lim_{k\to+\infty}\left|f_{lpf}\left(e_{ib}(k)\right)\right| - \Delta I_b\left(k+1\right) \geq 0. \tag{34}$$

Selecting a small enough B to make $|f_{lpf}(e_{ib}(k_0))| \geq \Delta I_b(k_0+1)$ at $k = k_0$. According to (33) and (31), it has

$$t_p\left(k_0\right) \geq t_p\left(k_0+1\right)$$

$$\Delta\xi\left(k_0\right) \geq \Delta\xi\left(k_0+1\right). \tag{35}$$

So (36) is satisfied

$$\Delta I_b\left(k_0+1\right) \geq \Delta I_b\left(k_0+2\right)$$

$$\sum_{n=1}^{n=+\infty}\Delta I_b\left(k_0+n\right) \leq \varepsilon, \varepsilon \propto B. \tag{36}$$

Hence, there existing a maximum B to guarantee

$$\left|f_{lpf}\left(e_{ib}\left(k_0\right)\right)\right| - \sum_{n=0}^{n=+\infty}\Delta I_b\left(k_0+n\right)$$

$$= \lim_{k\to+\infty}\left|f_{lpf}\left(e_{ib}(k)\right)\right| - \Delta I_b\left(k+1\right) \geq 0. \tag{37}$$

■

C. Adaptive Constraints and Model Active Mismatch in Power Control Loop

The overall control scheme for the proposed AC-MAMPC is shown in Fig. 1. The dynamic mode enable block is used to judge whether the system is in steady-state (1) or dynamic mode (0). In steady state, the inductance and constraints are changing based on (22) and (29), and the capacitance C keep the original value. The changing of inductance would eliminate the current ripple, and the adaptive variation of constraints about duty ratio can compensate the model-mismatch caused by the changing of inductance.

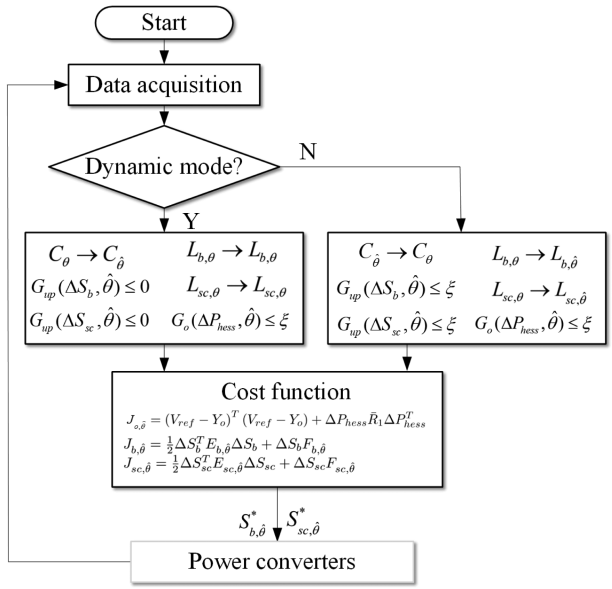

Fig. 4. Flowchart of AC-MAMPC.

In the dynamic mode, the increasing of inductance would lead to slower response, so the inductance of power converter and constraints about duty ratio would return back to the original value. Unlike the model active mismatch in current control loop that the inductance is rising, the capacitance C should decrease to enlarge the voltage ripple caused by control system in dynamic response, and the dynamic error can be reduced. The action model mismatch on capacitance is shown as

$$C_{\hat\theta} = C_\theta - B_1\left(\left|V_{\text{ref}} - v_o(k)\right|\right) \tag{38}$$

where B_1 is the active model mismatch parameters. Due to $C_{\hat\theta} = C_\theta$ when $v_o(k) = V_{\text{ref}}$, the overshoot caused by capacitance mismatch can be avoided.

For power control loop, the dynamic power losses and disturbance can lead to additional model mismatch, so, the constraints of (3) should be variation. The updating law of constraint about HESS power is designed as (39), which is as same as that of duty ratio

$$G_o\left(\Delta P_{\text{hess}}, \hat\theta\right) \leq -\xi_o$$

$$\xi_o(k) = \xi_o\left(k-1\right) + B_o \cdot \text{sign}\left[\frac{f_{lpf}\left(e_v(k)\right)}{e_v(k)}\right] \tag{39}$$

where $G_o(\Delta P_{\text{hess}}, \hat\theta)$ is the constraint about HESS power. The flowchart of AC-MAMPC can be seen in Fig. 4.

V. Simulation Results

In this section, the proposed method is verified through MATLAB/Simulink, the system parameters are shown in Table I. According to the analysis in Section III-A, the current ripple magnitude induced by control delay and model mismatch remains independent of the HESS power level, and in low power situation, the effects of current ripple and control track error become more pronounced in their impact on output voltage

TABLE I
SYSTEM PARAMETERS

Parameter	V_{ref}	v_b	v_{sc}	C
Normal Value	48V	24V	24V	$500\mu F$
Parameter	L_b,L_{sc}	f_s	f_{sw}	N_p,N_c
Normal Value	$3mH$	$10kHz$	$5kHz$	4,3

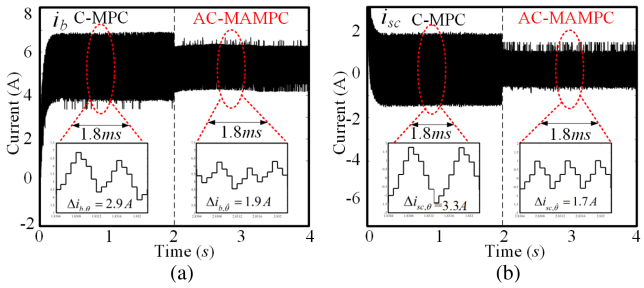

Fig. 5. Control performance of AC-MAMPC and C-MPC in steady state: (a) Battery current. (b) SC current.

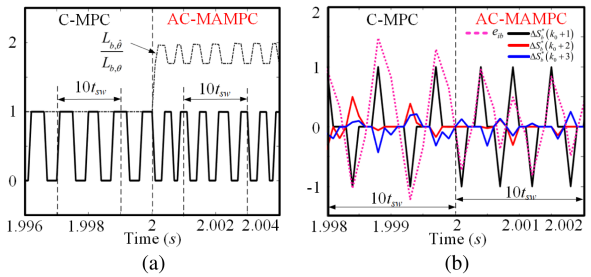

Fig. 6. Control performance of AC-MAMPC and C-MPC in steady state. (a) PWM signals and situation of active model mismatch. (b) Optimal solution $\Delta S^*_{b,\hat{\theta}}$ and the current tracing error e_{ib}.

regulation, hence, the simulation and hardware experiment in this article are all completed in low power level.

A. Case 1: The Comparison Between AC-MAMPC and C-MPC

Figs. 5 and 6 show the performance under the control of AC-MAMPC and C-MPC in steady state. The C-MPC is described in detail in Section II [25], [26]. In this case, i_b is around $5.5A$ and i_{sc} is $0A$. At $2s$, C-MPC is replaced by AC-MAMPC. Comparing with C-MPC, the current ripple of battery and SC is reduced by 34.5% and 48.5%, respectively.

It can be seen in Fig. 6(a), within 10 switching period, the control actions changes 5 times and 7 times under the control of C-MPC and AC-MAMPC. Because of the active model-mismatch for dc–dc inductance, the optimization delay can be compensated. Fig. 6(b) shows the comparison of optimal solution $\Delta S^*_{b,\hat{\theta}}$ and the current tracing error e_{ib}. Under the control of AC-MAMPC, the online optimization process can response to the tracing error fast and frequently. Hence, the current ripple can be reduced significantly.

Fig. 7 shows the dynamic performance of AC-MAMPC, at 5 s, the power requirement of load is changed form 46 to 154 W. According to Fig. 7(a), the voltage ripple of AC-MAMPC is

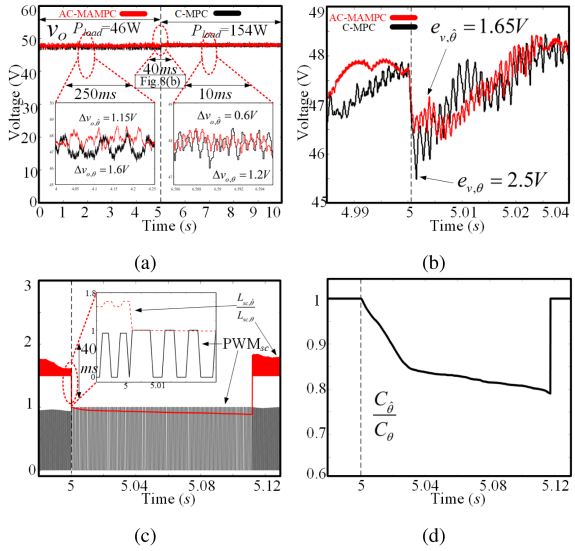

Fig. 7. Control performance of AC-MAMPC and C-MPC in dynamic response. (a) DC bus voltagev_o. (b) Dynamic error on v_o. (c) Variation of PWM and inductance of SC DC–DC converter. (d) Variation of capacitance.

reduced by 28.1% and 50.0% compared with C-MPC. Fig. 7(b) shows the variation of dc bus voltage v_o when the load demand is changing suddenly, the dynamic error of AC-MAMPC is decreasing by 34.0%. From Fig. 7(c) and (d), to achieve the fast dynamic response, the capacitance of dc–dc converter connected with SC and the capacitance are decreasing actively, and the constraint of duty ratio back to $[0, 1]$ again.

B. Case 2: The Performance of Adaptive Constraints Mechanism

To demonstrate that the proposed method can deal with the plants mismatch problem, MPC method with active model mismatch mechanism (MAMPC) is used to make comparison with the proposed AC-MAMPC in this case study. p_{loss} is set as 0, so the power loss of energy conversion can be seen as the disturbance in power control loop. Under the condition of lower HESS current level, the effect of model mismatch is more obvious, so P_{pv} and P_{load} are set as 48 W and 46 W in this case study, and the charging current of HESS is near to 0. Fig. 8(a)–(c) shows the track error of dc bus voltage and HESS current. In power control loop, MAMPC has 0.2 V steady-state error because of power loss. In current control loop, MAMPC has 0.15 A and -0.1 A steady-state error in i_b and i_{sc}. The proposed method can against these disturbances by constraints adaption. The constraints adaption can be seen in Fig. 8(d)–(f).

C. Case 3: The Performance of AC-MAMPC Under Constant Power Load (CPL) Application

In this case, the proposed AC-MAMPC is tested under CPL conditions. Since the proposed method does not include an estimator for the negative resistance characteristic of CPL, the CPL issue can be treated as a type of model mismatch problem. Fig. 9 illustrates the dynamic and steady-state performance of AC-MAMPC and C-MPC.

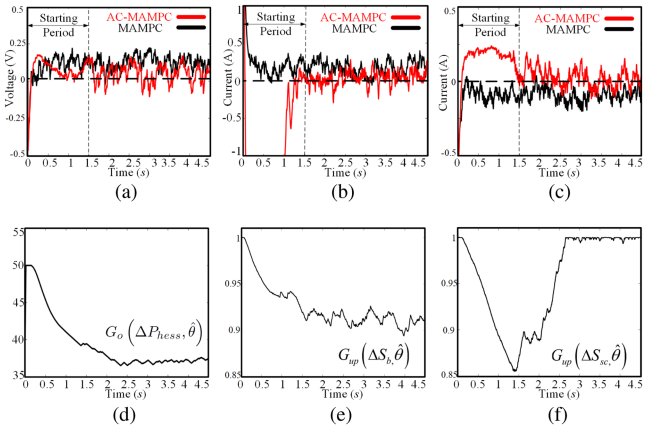

Fig. 8. Control performance under the disturbances. (a) $f_{\text{lpf}}(e_o)$. (b) $f_{\text{lpf}}(e_{ib})$. (c) $f_{\text{lpf}}(e_{\text{isc}})$. (d) Constraint for maximum HESS power. (e) Constraint for maximum duty ratio of battery DC–DC converter. (f) Constraint for maximum duty ratio of SC DC–DC converter.

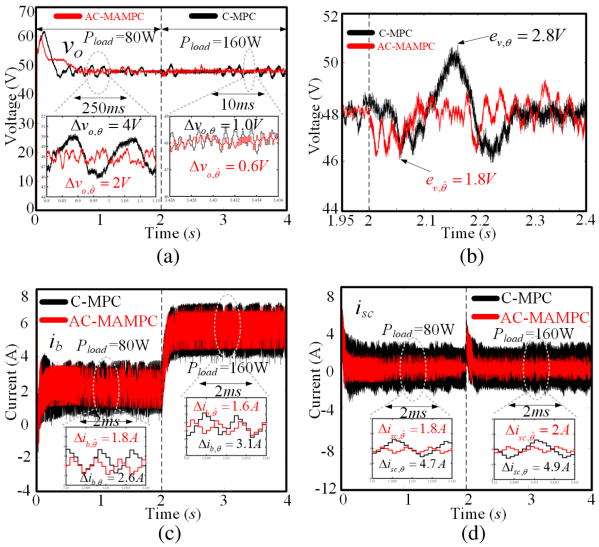

Fig. 9. Control performance under CPL. (a) DC bus voltage v_o. (b) Dynamic error on v_o. (c) Battery current. (d) SC current.

Fig. 9(a) and (b) depicts the variation of v_o when the P_{load} switches from 80 to 160 W. Without the consideration of CPL, there are large current ripple, dynamic error, and settling time under the control of C-MPC. Comparing with C-MPC, the voltage ripple of AC-MAMPC is reduced by 50% and 40% during steady-state operation, respectively. When a sudden change occurs in the P_{load}, the dynamic error of the AC-MAMPC method decreases by 35.7%. Fig. 9(c) and (d) compares the current ripples of i_b and i_{sc} under the two methods. Before and after the CPL transitions, the AC-MAMPC method achieves reductions in current ripple of i_b and i_{sc} by 30.7%, 48.3%, and 61.7%, 59.1%, respectively.

D. Case 4: The Performance Comparison of AC-MAMPC and ESO-MPC Under CPL

Fig. 10 compares the control performance in the CPL scenario of AC-MAMPC and ESO-MPC reported in [28] and [29].

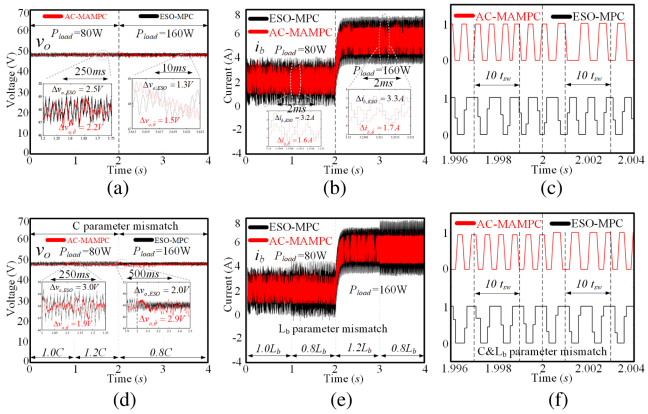

Fig. 10. Control performance under CPL. (a) DC bus voltage v_o. (b) Battery current. (c) Variation of PWM of battery DC–DC converter. (d) DC bus voltage v_o under model mismatch. (e) Battery current under model mismatch. (f) Variation of PWM of battery DC–DC converter under model mismatch.

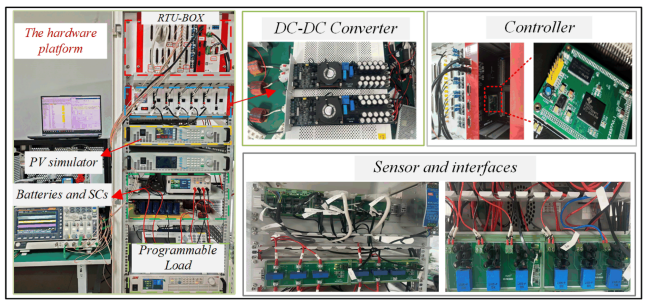

Fig. 11. Hardware platform.

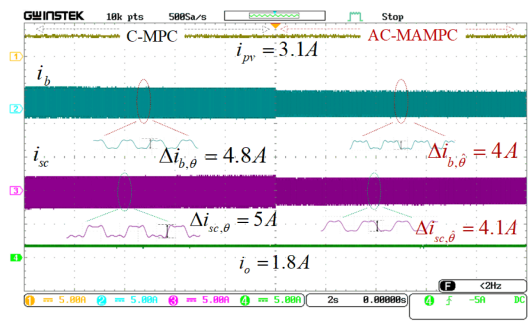

Fig. 12. Control performance of AC-MAMPC and C-MPC in steady state.

Fig. 10(a) and (b) describes the variation in v_o and i_b as the P_{load} varies from 80 to 160 W. Compared to ESO-MPC, the battery current ripple is reduced by 50% and 48.5% under the control of AC-MAMPC. Fig. 10(c) demonstrates the control actions of AC-MAMPC changes more frequently than that of ESO-MPC, which means the optimization delay is eliminated. Fig. 10(d) and (e) shows the control performance under model mismatch conditions and CPL. By altering the capacitance and battery inductance in the system model, it is observed that the ESO-MPC has a good performance on output voltage, but the battery current ripple of AC-MAMPC remains less, thus verifying that the adaptive constraint mechanism can effectively handle model mismatch issues. Fig. 10(f) illustrates that ESO-MPC still has optimization delay problem.

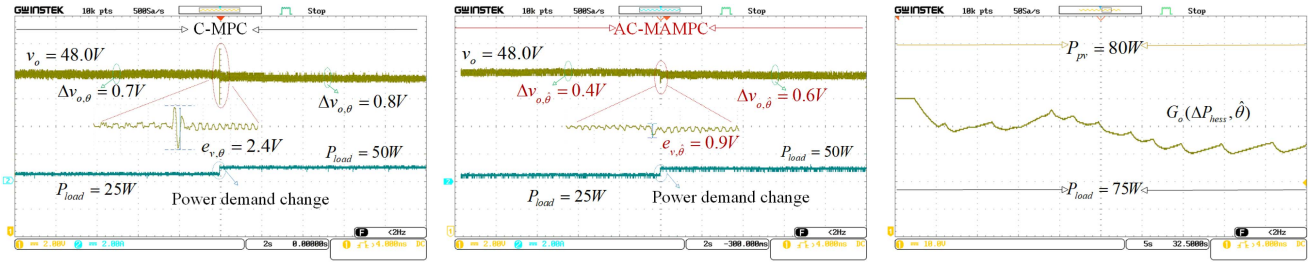

(a) (b) (c)

Fig. 13. (a) Control performance of C-MPC in dynamic response. (b) Control performance of AC-MAMPC in dynamic response. (c) Constraint variation about HESS power.

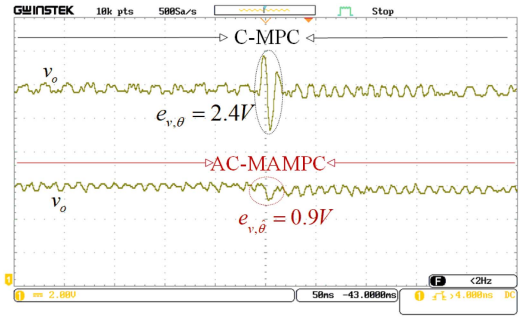

Fig. 14. Comparison of magnified voltage waveforms from Fig. 13(a) and (b).

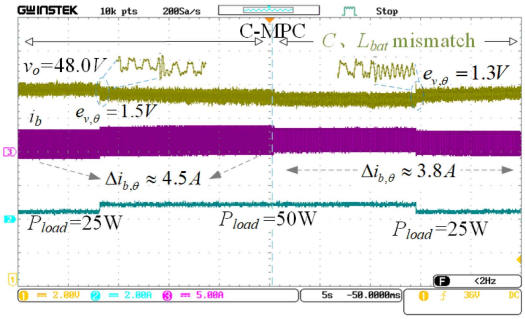

Fig. 15. Performance comparison of C-MPC under model mismatch.

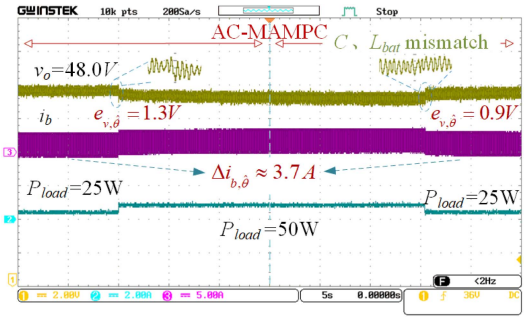

Fig. 16. Performance comparison of AC-MAMPC under model mismatch.

VI. Hardware Experimental Results

In this section, the proposed algorithm is validated using a hardware experimental platform, as shown in Fig. 11. RTU-BOX206 is used as the microcontroller, and the system sampling frequency f_s is 5 kHz. For HESS system, two sets of six series-connected SCs (Maxwell, 2.7 V, 350 Farads each) are connected in parallel, and two 12 V 1.8 Ah lithium batteries are connected in series. Subsequently, dc–dc converters are constructed using silicon carbide (SiC).

A. Case 1: The Performance Comparison of C-MPC and AC-MAMPC

Fig. 12 illustrates the steady-state control performance of C-MPC and AC-MAMPC on the hardware experimental platform. In this scenario, the HESS operates in a discharging state, with the i_b maintained at approximately 1.45 A and the i_{sc} at 0 A. At 1 s, the control strategy transitions from C-MPC to AC-MAMPC. Compared to C-MPC, the current ripple of the battery and SC decreases by 16.7% and 18%, respectively. Fig. 13(a) and (b), respectively, presents the dynamic control performance of C-MPC and AC-MAMPC under a load disturbance scenario. At 1 s, the power load demand transitions from 25 to 50 W. It can be observed that the voltage ripple of AC-MAMPC is reduced by 42.8% and 25.0% compared with C-MPC. To verify the effectiveness of the adaptive constraint mechanism, Fig. 13(c) demonstrates the dynamic variation of the power loop constraint during the control process to compensate the model-mismatch problem. Fig. 14 shows the dynamic response during a sudden load change, where AC-MAMPC achieves a 62.5% reduction in dynamic error compared to C-MPC.

B. Case 2: The Performance Comparison of C-MPC and AC-MAMPC Under Model Mismatch

Figs. 15 and 16 show the control performance of C-MPC and AC-MAMPC under model mismatch conditions. In the left half of Fig. 15, the P_{load} abruptly changes from 25 to 50 W without any model mismatch. In the right half of Fig. 15, the P_{load} decreases from 50 to 25 W, while the C and L_b parameters in the system model experience a mismatch. A comparison reveals that C-MPC results in significant changes in battery current ripple under model mismatch. Fig. 16 demonstrates that AC-MAMPC maintains a stable and well-controlled battery current ripple even under load fluctuations and model mismatch.

C. Case 3: The Performance Comparison of C-MPC, AC-MAMPC, and ESO-MPC

Fig. 17(a)–(c) compares the battery current ripple and v_o of C-MPC, AC-MAMPC, and ESO-MPC under the same load fluctuation. The comparison shows that AC-MAMPC exhibits

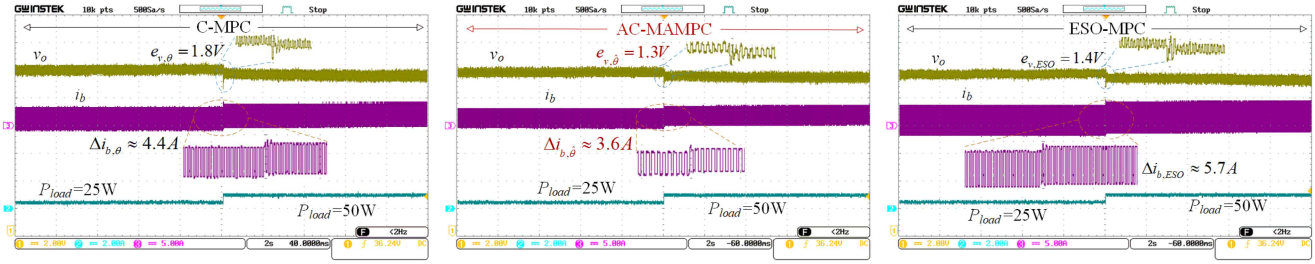

(a) (b) (c)

Fig. 17. Control performance of C-MPC, AC-MAMPC and ESO-MPC. (a) Control performance of C-MPC. (b) Control performance of AC-MAMPC. (c) Control performance of ESO-MPC.

the best performance in terms of battery current ripple and dynamic error of v_o.

VII. Discussion

The proposed AC-MAMPC method reduces current ripple by eliminating the control delay inherent in C-MPC. In addition, the proposed adaptive constraints method addresses model-mismatch issues, while the ESO-based approach treats all mismatches and unmodeled dynamics as a lumped disturbance for compensation. From a theoretical perspective, these two methods do not conflict and could be jointly employed to achieve better control outcomes. Also, AC-MAMPC may affect dynamic performance under certain circumstances, in the future work, it could be integrated with event-triggered mechanisms to address such issues.

VIII. Conclusion

This article presents an AC-MAMPC method to address trajectory tracking errors of C-MPC method for power converters caused by limited sampling frequency and model mismatches. The method actively adjusts system model parameters to reduce current ripple and introduces an adaptive constraints approach for online optimization with simplest system model. Experimental and comparative results demonstrate the effectiveness of the proposed control method. Comparing with C-MPC, the voltage and current ripples are reduced by 25%–42.8% and 16.7%–18%, respectively, in steady state, and the dynamic error and settling time are decreased by 62.5% and 37.5%.

References

[1] L. Deng, G. Zhou, Y. Li, and Z. Chen, "Communication-free pulsed power distribution and tracking method for hybrid energy storage system based on active disturbance rejection control," *IEEE Trans. Power Electron.*, vol. 39, no. 3, pp. 3024–3036, Mar. 2023.

[2] P. Karamanakos, E. Liegmann, T. Geyer, and R. Kennel, "Model predictive control of power electronic systems: Methods, results, and challenges," *IEEE Open J. Ind. Appl.*, vol. 1, pp. 95–114, 2020.

[3] V. Jayan and A. M. Y. M. Ghias, "Computationally-efficient model predictive control of dual-output multilevel converter in hybrid microgrid," *IEEE Trans. Power Electron.*, vol. 38, no. 5, pp. 5898–5910, May 2023.

[4] Y. Shan, J. Hu, K. W. Chan, Q. Fu, and J. M. Guerrero, "Model predictive control of bidirectional DC–DC converters and AC/DC interlinking converters—a new control methodfor PV-wind-battery microgrids," *IEEE Trans. Sustain. Energy*, vol. 10, no. 4, pp. 1823–1833, Oct. 2018.

[5] Q. Song, L. Wang, and J. Chen, "A decentralized energy management strategy for a fuel cell–battery hybrid electric vehicle based on composite control," *IEEE Trans. Ind. Electron.*, vol. 68, no. 7, pp. 5486–5496, Jul. 2020.

[6] Z. Karami, Q. Shafiee, S. Sahoo, M. Yaribeygi, H. Bevrani, and T. Dragicevic, "Hybrid model predictive control of DC–DC boost converters with constant power load," *IEEE Trans. Energy Convers.*, vol. 36, no. 2, pp. 1347–1356, Jun. 2020.

[7] Z. Song et al., "Simultaneous identification and control for hybrid energy storage system using model predictive control and active signal injection," *IEEE Trans. Ind. Electron.*, vol. 67, no. 11, pp. 9768–9778, Nov. 2019.

[8] A. Ortiz, P. Lezana, and M. Norambuena, "Two stages FCS-MPC for a flying capacitor converter with improved switching performance," *IEEE Trans. Ind. Informat.*, vol. 20, no. 6, pp. 8358–8367, Jun. 2024.

[9] X. Liu, Y. Suo, Z. Zhang, X. Song, and J. Zhou, "A new model predictive current control strategy for hybrid energy storage system considering the SOC of the supercapacitor," *IEEE Trans. Emerg. Sel. Topics Power Electron.*, vol. 11, no. 1, pp. 325–338, Feb. 2022.

[10] L. Zhou and M. Preindl, "Variable-switching constant-sampling frequency critical soft switching MPC for DC/DC converters," *IEEE Trans. Energy Convers.*, vol. 36, no. 2, pp. 1548–1561, Jun. 2021.

[11] B. Zhang et al., "Enhanced deadbeat control-model predictive control strategy of grid-connected power converters with LCL filter," *IEEE Trans. Ind. Electron.*, vol. 71, no. 12, pp. 15826–15834, Dec. 2024.

[12] H. Lin, H. S.-H. Chung, R. Shen, and Y. Xiang, "Enhancing stability of DC cascaded systems with CPLs using MPC combined with Ni and accounting for parameter uncertainties," *IEEE Trans. Power Electron.*, vol. 39, no. 5, pp. 5225–5238, May 2024.

[13] Z. Dong, Q. Chen, J. Qin, Z. Zhang, K. T. Chi, and Y. Xu, "Noise tolerance strategy based on virtual capacitor for DC–DC converters with continuous control set model predictive control," *IEEE Trans. Power Electron.*, vol. 39, no. 8, pp. 9084–9088, Aug. 2024.

[14] A. Brosch, O. Wallscheid, and J. Böcker, "Long-term memory recursive least squares online identification of highly utilized permanent magnet synchronous motors for finite-control-set model predictive control," *IEEE Trans. Power Electron.*, vol. 38, no. 2, pp. 1451–1467, Feb. 2022.

[15] S. Niu, Y. Luo, W. Fu, and X. Zhang, "Robust model predictive control for a three-phase PMSM motor with improved control precision," *IEEE Trans. Ind. Electron.*, vol. 68, no. 1, pp. 838–849, Jan. 2020.

[16] L. Tao, P. Wang, X. Ma, Y. Wang, and H. Shi, "Robustness optimization through modified linear active disturbance rejection control for high-voltage load interface in microgrid," *IEEE Trans. Ind. Electron.*, vol. 70, no. 4, pp. 3909–3919, Apr. 2022.

[17] S. K. Panda and B. Subudhi, "An extended state observer based adaptive backstepping controller for microgrid," *IEEE Trans. Smart Grid*, vol. 15, no. 1, pp. 171–178, Jan. 2023.

[18] X. Liu, L. Qiu, Y. Fang, K. Wang, Y. Li, and J. Rodríguez, "A two-step event-triggered-based data-driven predictive control for power converters," *IEEE Trans. Ind. Electron.*, vol. 71, no. 11, pp. 13545–13555, Nov. 2024.

[19] N. Jin, M. Chen, L. Guo, Y. Li, and Y. Chen, "Double-vector model-free predictive control method for voltage source inverter with visualization analysis," *IEEE Trans. Ind. Electron.*, vol. 69, no. 10, pp. 10066–10078, Oct. 2021.

[20] Y. Zhang, J. Jin, and L. Huang, "Model-free predictive current control of PMSM drives based on extended state observer using ultralocal model," *IEEE Trans. Ind. Electron.*, vol. 68, no. 2, pp. 993–1003, Feb. 2020.

[21] O. Babayomi, Z. Zhang, and Z. Li, "Model-free predictive control of DC–DC boost converters: Sensor noise suppression with hybrid extended state observers," *IEEE Trans. Power Electron.*, vol. 39, no. 1, pp. 245–259, Jan. 2023.
[22] Q. Yang, J. Zhou, X. Chen, and J. Wen, "Distributed MPC-based secondary control for energy storage systems in a DC microgrid," *IEEE Trans. Power Syst.*, vol. 36, no. 6, pp. 5633–5644, Jun. 2021.
[23] Y. Wei, H. Young, F. Wang, and J. Rodríguez, "Generalized data-driven model-free predictive control for electrical drive systems," *IEEE Trans. Ind. Electron.*, vol. 70, no. 8, pp. 7642–7652, Aug. 2022.
[24] J. Gao, C. Gong, W. Li, and J. Liu, "Novel compensation strategy for calculation delay of finite control set model predictive current control in PMSM," *IEEE Trans. Ind. Electron.*, vol. 67, no. 7, pp. 5816–5819, Jul. 2019.
[25] X. Zhang, B. Wang, D. Gamage, and A. Ukil, "Model predictive and iterative learning control based hybrid control method for hybrid energy storage system," *IEEE Trans. Sustain. Energy*, vol. 12, no. 4, pp. 2146–2158, Oct. 2021.
[26] B. Wang, V. R. K. Kanamarlapudi, L. Xian, X. Peng, K. T. Tan, and P. L. So, "Model predictive voltage control for single-inductor multiple-output DC–DC converter with reduced cross regulation," *IEEE Trans. Ind. Electron.*, vol. 63, no. 7, pp. 4187–4197, Jul. 2016.
[27] B. Chachuat, A. Marchetti, and D. Bonvin, "Process optimization via constraints adaptation," *J. Process Control*, vol. 18, no. 3/4, pp. 244–257, 2008.
[28] K. Zhao, Y. Wei, Y. Hou, T. Yang, J. Wu, and Y. Xie, "The optimal tracking control for autonomous underwater vehicles using ESO and MPC algorithms," in *Proc. OCEANS*, 2024, pp. 1–10.
[29] H. Liu and S. Li, "Speed control for PMSM servo system using predictive functional control and extended state observer," *IEEE Trans. Ind. Electron.*, vol. 59, no. 2, pp. 1171–1183, Feb. 2011.

Xibeng Zhang (Member, IEEE) received the B.E. degree in electronic information engineering from Zhengzhou University, Zhengzhou, China, in 2016, and the M.S. and Ph.D. degrees in electrical engineering from the University of Auckland, Auckland, New Zealand, in 2018 and 2022, respectively.

He is currently an Assistant Professor with the School of Artificial Intelligence, Henan University, Kaifeng, China. His research interests include photovoltaics, dc microgrids, and hybrid energy storage systems.

Shun Zhou is currently working toward the master's degree in artificial intelligence with Henan University, Kaifeng, China.

His research interests focus on electro-hydrogen coupled microgrids.

Benfei Wang (Senior Member, IEEE) received the B.Sc. degree in electronic information science and technology from the University of Science and Technology of China, Hefei, China, in 2011, and the Ph.D. degree in electrical and electronic engineering from Nanyang Technological University (NTU), Singapore, in 2017.

From 2017 to 2019, he was Postdoctoral Research Fellow with the Energy Research Institute, NTU. He is currently an Associate Professor with the School of Intelligent Systems Engineering, Sun Yat-Sen University, Guangzhou, China. His research interests include model predictive control, multiport converter, energy storage system, electric vehicles, and microgrids.

Dr. Wang is currently an Associate Editor for IEEE TRANSACTIONS ON INDUSTRIAL ELECTRONICS, Guest Associate Editor for IEEE JOURNAL OF EMERGING AND SELECTED TOPICS IN INDUSTRIAL ELECTRONICS, and Youth Editor of The Innovation Energy.

Yang Lu received the Ph.D. degree in civil engineering from the College of Civil Engineering, Tongji University, Shanghai, China, in 2008.

She is currently the Dean and a Professor with the School of Artificial Intelligence, Henan University, Kaifeng, China. Her research interests focus on controlling of energy systems.

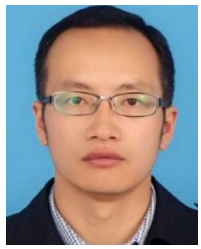

Yanyu Zhang received the B.S. degree in automation from Henan University, Kaifeng, China, in 2003, the M.S. degree in mechatronic engineering from the Graduate School of Chinese Academy of Sciences, Beijing, China, in 2006, and the Ph.D. degree in mechatronic engineering from the University of Chinese Academy of Sciences, Beijing, China, in 2016.

He is currently an Associate Professor with the School of Artificial Intelligence, Henan University. His research interests include energy management systems and deep learning.

Feng Huo received the Ph.D. degree in chemical engineering from the Beijing University of Chemical Technology, Beijing, China, in 2013.

He then joined the Institute of Process Engineering, Chinese Academy of Sciences, Beijing, China, as a Postdoctoral Researcher. His research focuses on green chemical engineering and the system integration of hydrogen-electric coupling microgrids.

Dr. Huo was the recipient of the Ionic Liquid and Green Processes New Talent Award, in 2017. In 2019, he was selected as a member of the "Process Excellent Youth" at the CAS Institute of Process Engineering.

Darong Huang (Member, IEEE) received the B.S. degree in applied mathematics from the Hubei National Institute, Enshi, China, in 2000, the M.S. degree in applied mathematics from Liaoning University, Shenyang, China, in 2003, and the Ph.D. degree in control theory and control engineering from Chongqing University, Chongqing, China, in 2006.

He is with the Engineering Research Center of Autonomous Unmanned System Technology of Ministry of Education, Anhui Provincial Engineering Research Center for Unmanned System and Intelligent Technology, and the School of Artificial Intelligence, Anhui University, Hefei, China.

Abhisek Ukil (Senior Member, lEEE) received the B.E. degree in electrical engineering from Jadavpur University, Kolkata, India, in 2000, the M.Sc. degree in electronic systems from the University of Bolton, Bolton, U.K., in 2004, and the Ph.D. degree in electrical and electronic engineering from the Pretoria University of Technology, Pretoria, South Africa, in 2006.

He is currently an Associate Professor with the Department of Electrical, Computer, and Software Engineering, The University of Auckland, Auckland, New Zealand. His research interests include smart grids and power system automation.